SAND2017-5347J

Modeling Shockwaves and Impact Phenomena with Eulerian Peridynamics

Stewart A. Silling, Michael L. Parks, James R. Kamm
Center for Computing Research
Sandia National Laboratories
Albuquerque, New Mexico USA

Olaf Weckner, Mostafa Rassaian
The Boeing Company
Seattle, Washington USA

Abstract

Most previous development of the peridynamic theory has assumed a Lagrangian formulation, in which the material model refers to an undeformed reference configuration. In the present work, an Eulerian form of material modeling is developed, in which bond forces depend only on the positions of material points in the deformed configuration. The formulation is consistent with the thermodynamic form of the peridynamic model and is derivable from a suitable expression for the free energy of a material. It is shown that the resulting formulation of peridynamic material models can be used to simulate strong shock waves and fluid response in which very large deformations make the Lagrangian form unsuitable. The Eulerian capability is demonstrated in numerical simulations of ejecta from a wavy free surface on a metal subjected to strong shock wave loading. The Eulerian and Lagrangian contributions to bond force can be combined in a single material model, allowing strength and fracture under tensile or shear loading to be modeled consistently with high compressive stresses. This capability is demonstrated in numerical simulation of bird strike against an aircraft, in which both tensile fracture and high pressure response are important.

Keywords: Shockwave, Spall, Peridynamic, Nonlocal, Birdstrike
2010 MSC: 74J35, 74B20

1. Introduction

Nearly all work on peridynamics up to now has assumed material models that are *Lagrangian*, meaning that the bond forces depend not only on the current (deformed) configuration of the body, but also on a reference (undeformed) configuration. An exception is the class of *structureless* material models that were considered in [1]. These materials have bond force densities that are independent of any reference configuration, but, due to additional assumptions in what is now called the *bond-based* peridynamic theory, the structureless materials were found to have very restrictive properties and are generally not useful in applications.

In the present work, we re-examine the possibility of peridynamic material models that depend only on the deformed configuration, but do so within the *state-based* theory. It is shown that the greater generality of the state-based theory compared with the earlier bond-based theory avoids all of the limitations of the structureless materials. When incorporated within the thermodynamic statement of peridynamics, material models in the state-based theory can use any equation of state from the standard (local) theory. Futhermore, the resulting material models, which will be called *Eulerian*, can be combined in a straightforward way with Lagrangian models. This provides a convenient way to model solids in applications that involve fracture and fragmentation under tensile or shear loading, in which a Lagrangian formulation is the natural approach, with high pressures and large deformations, in which an Eulerian model has advantages. The capabilities of the Eulerian approach to peridynamic material modeling are demonstrated with examples from shock wave physics and impact mechanics of soft materials.

In Section 2 we provide a brief overview of the peridynamic theory, including mechanics and thermodynamics. In Section 3 we introduce a peridynamic Eulerian model equipped with a Mie-Grüneisen equation-of-state. Application to shockwave ejecta in a metal subjected to a detonation wave is presented in Section 3.4, along with comparison with experiment. Combination of Eulerian and

Lagrangian contributions to bond force density in a material model is discussed in Section 4. This approach is demonstrated in a problem involving comminution of a material followed by large compression in Section 4.1. Simulation of birdstrike, along with validation of the predicted centerline pressure history, is described in Section 5. It is shown that the contribution of the Lagrangian terms, even though the problem appears to be dominated by large pressures at the point of impact, significantly improve the prediction of how the projectile shape evolves.

2. Peridynamic theory summary

Here we review key features and equations of the peridynamic theory, including the mechanical theory and thermodynamics. A more detailed discussion may be found in the review article [2]. The numerical discretization method used for all the examples in the present paper is described in the Appendix.

2.1. Mechanics

The classical momentum equation for solid mechanics in Lagrangian form is

$$\rho_0(\mathbf{x})\ddot{\mathbf{y}}(\mathbf{x},t) = \nabla\cdot\boldsymbol{\sigma}(\mathbf{x},t) + \mathbf{b}(\mathbf{x},t) \tag{1}$$

where ρ_0 is the mass density in the reference configuration, $\mathbf{x}$ is a material point in the reference configuration, $\mathbf{y}$ is the deformation map, $\nabla\cdot$ is the divergence operator, $\boldsymbol{\sigma}$ is the Piola stress tensor field, and $\mathbf{b}$ is the body force density field.

The primary motivations for development of the peridynamic theory arise from the inapplicability of the PDE (1) at cracks or crack tips due to the nonexistence of the necessary spatial derivatives on these singularities, and the inability of this equation to include long-range forces. Since (1) cannot be applied directly on discontinuites, special techniques such as XFEM [3] have been proposed to insert cracks into discretized regions that are assumed to undergo smooth deformation elsewhere. Although these special techniques have achieved many

successes, they require additional complexity, including supplemental equations that dictate the crack growth velocity and direction.

In contrast, the peridynamic theory of solid mechanics is based on integral equations, for which discontinuous solutions present no difficulty [1, 4]. In peridynamics, cracks nucleate, grow, branch, merge, and arrest when and where it is energetically favorable for them to do so according to the basic field equations and material model. This capability for *autonomous crack growth* avoids the need for the special techniques of fracture mechanics. See [5] for a comparison of peridynamics with cohesive zone methods and XFEM. Peridynamics has been successfully applied to model fracture in polycrystals [6], failure and fracture in composites [7], dynamic brittle fracture in glass [8], and failure in electronic packages due to drop-shock [9], among other applications. As a multiscale material model, peridynamics has been demonstrated to be an upscaling of molecular dynamics [10]. It has been implemented within a massively parallel open-source molecular dynamics code [11], demonstrating scalable computational performance on a computer with 65,000 processors.

In the peridynamic model, any material point $\mathbf{x}$ interacts through the material model with its neighbors $\mathbf{q}$ within a prescribed distance δ of itself in the reference configuration. This maximum interaction distance δ is called the *horizon*, and the material within the horizon of $\mathbf{x}$ in the reference configuration is called the *family* of $\mathbf{x}$, denoted $\mathcal{H}_{\mathbf{x}}$. The vector between $\mathbf{x}$ and any point $\mathbf{q}$ in its family is called a *bond*, denoted $\mathbf{q}-\mathbf{x}$. Figure 1 illustrates the horizon and family of $\mathbf{x}$. Associated with each bond is a *pairwise bond force density vector* (force per unit volume squared) that $\mathbf{q}$ exerts on $\mathbf{x}$, denoted $\mathbf{f}(\mathbf{q},\mathbf{x},t)$. The peridynamic equation of motion is

$$\rho_0(\mathbf{x})\ddot{\mathbf{y}}(\mathbf{x},t) = \int_{\mathcal{H}_{\mathbf{x}}} \mathbf{f}(\mathbf{q},\mathbf{x},t)\, dV_{\mathbf{q}} + \mathbf{b}(\mathbf{x},t). \tag{2}$$

The pairwise bond force density function is antisymmetric:

$$\mathbf{f}(\mathbf{x},\mathbf{q},t) = -\mathbf{f}(\mathbf{q},\mathbf{x},t), \tag{3}$$

which ensures that linear momentum is globally balanced.

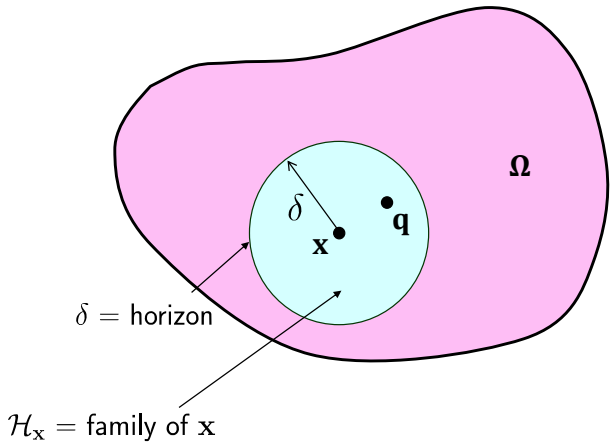

Figure 1: A typical material point $\mathbf{x}$ interacts with its neighbors $\mathbf{q}$ within its horizon.

The bond forces are determined jointly by the collective deformation of $\mathcal{H}_{\mathbf{x}}$ and the collective deformation of $\mathcal{H}_{\mathbf{q}}$. To precisely describe these collective deformations, a mathematical formalism involving objects called *states* is used. States are operators that act on bonds. For present purposes, states are vector valued, that is, if $\underline{\mathbf{A}}$ is a state, then $\underline{\mathbf{A}}\langle \mathbf{q}-\mathbf{x}\rangle$ is a vector. The inner product of any two states $\underline{\mathbf{A}}$ and $\underline{\mathbf{B}}$ is defined by

$$\underline{\mathbf{A}} \bullet \underline{\mathbf{B}} = \int_{\mathcal{H}_{\mathbf{x}}} \underline{\mathbf{A}}\langle \mathbf{q}-\mathbf{x}\rangle \cdot \underline{\mathbf{B}}\langle \mathbf{q}-\mathbf{x}\rangle \, dV_{\mathbf{q}}.$$

States are the nonlinear analogues of second order tensors in linear algebra, which are linear transformations that map vectors to vectors. For functions of states, Fréchet derivatives are used instead of tensor gradients. To define the Fréchet derivative, let Ψ be a scalar-valued function of a vector state $\underline{\mathbf{A}}$. Suppose there is a state denoted $\Psi_{\underline{\mathbf{A}}}$ such that for any increment $\Delta\underline{\mathbf{A}}$,

$$\Psi(\underline{\mathbf{A}} + \Delta\underline{\mathbf{A}}) = \Psi(\underline{\mathbf{A}}) + \Psi_{\underline{\mathbf{A}}} \bullet \Delta\underline{\mathbf{A}} + o(\|\Delta\underline{\mathbf{A}}\|) \tag{4}$$

where

$$\|\Delta\underline{\mathbf{A}}\| = \sqrt{\Delta\underline{\mathbf{A}} \bullet \Delta\underline{\mathbf{A}}}.$$

Then $\Psi_{\underline{\mathbf{A}}}$ is the Fréchet derivative of Ψ. For a more complete discussion of states, see [4].

For purposes of material modeling, the basic kinematical quantity is the *deformation state* $\underline{\mathbf{Y}}$, defined at any $[\mathbf{x}, t]$ by

$$\underline{\mathbf{Y}}[\mathbf{x}, t]\langle \mathbf{q}-\mathbf{x}\rangle = \mathbf{y}(\mathbf{q}, t) - \mathbf{y}(\mathbf{x}, t). \tag{5}$$

The deformation state maps bonds onto their images under the deformation and is analogous to the deformation gradient tensor in the classical theory.

Pairwise bond force densities are assigned through the *force state* $\underline{\mathbf{T}}$:

$$\mathbf{f}(\mathbf{q}, \mathbf{x}, t) = \underline{\mathbf{T}}[\mathbf{x}, t]\langle \mathbf{q}-\mathbf{x}\rangle - \underline{\mathbf{T}}[\mathbf{q}, t]\langle \mathbf{x}-\mathbf{q}\rangle.$$

In this equation, there are contributions from the force states at both endpoints of the bond $\mathbf{q}-\mathbf{x}$. Clearly this expression for $\mathbf{f}$ satisfies the required antisymmetry (3). The material model $\hat{\underline{\mathbf{T}}}$ prescribes the force state as a function of the

deformation state:

$$\underline{\mathbf{T}}[\mathbf{x},t] = \hat{\underline{\mathbf{T}}}(\underline{\mathbf{Y}}[\mathbf{x},t]), \qquad \underline{\mathbf{T}}[\mathbf{q},t] = \hat{\underline{\mathbf{T}}}(\underline{\mathbf{Y}}[\mathbf{q},t]). \tag{6}$$

The equations (6) show the main motivation for using the state formalism: instead of a material model that gives a tensor-valued function of a tensor, in peridynamics we have a state-valued function of a state. The material model may include dependencies on other variables such as temperature or the time derivative of $\underline{\mathbf{Y}}$. A particularly useful material model is the *elastic* material:

$$\underline{\mathbf{T}} = \hat{\underline{\mathbf{T}}}(\underline{\mathbf{Y}}) = W_{\underline{\mathbf{Y}}}(\underline{\mathbf{Y}})$$

where W is the *strain energy density function* for the material. Elastic peridynamic material models conserve energy in the usual sense: the total strain energy plus total kinetic energy in a body equals the net work done on the body through external loading.

Many peridynamic analogues of classical material models have been developed, including isotropic linear elastic [4], elastic-plastic [12], and viscoelastic [13] models. It can be shown that any material model in the classical theory can be used within the peridynamic theory [4].

In the limit as the peridynamic horizon approaches zero, the first term on the right-hand side of (2) has been proven to converge to the divergence of a Piola stress tensor that is a function only of the local deformation gradient tensor, as in the classical theory [14]. This limiting Piola stress tensor field is differentiable and obeys the classical partial differential equation for the equation of motion. The limiting, or *collapsed*, stress-strain model is elastic and obeys the conditions in the classical theory for angular momentum balance, isotropy, and objectivity, provided the original peridynamic material model satisfies these conditions. In this sense, peridynamics is a nonlocal extension of classical continuum mechanics.

In the peridynamic theory, damage is incorporated directly into a material model. For application to crack growth in solids, damage is included in the material model by allowing bonds to break. For example, a peridynamic bond

failure rule may specify that bonds are broken irreversibly when their elongation exceeds a prescribed critical value. After a bond breaks, the endpoints of the bond are effectively disconnected from each other, and the force that the bond was carrying is redistributed to other bonds that have not yet broken. This increased load makes it more likely that these other bonds will break, leading to progressive failure and crack propagation when this is energetically favorable. The work required to break a bond is determined by the critical energy release rate, an experimentally determinable quantity for brittle solids.

2.2. Thermodynamics

In the peridynamic formulation of thermodynamics, the first law expression at any material point $\mathbf{x}$ is given by

$$\dot{\varepsilon} = \underline{\mathbf{T}} \bullet \underline{\dot{\mathbf{Y}}} + q + Q \tag{7}$$

where ε is the internal energy density (per unit volume in the reference configuration), q is the rate of heat transport to $\mathbf{x}$ from other material points in the body, and Q is the source rate. The term $\underline{\mathbf{T}} \bullet \underline{\dot{\mathbf{Y}}}$ is called the *absorbed power density*, the peridynamic equivalent of the classical stress power. The second law expression for peridynamics is given by

$$\theta\dot{\eta} \geq q + Q$$

where η is the entropy density and θ is absolute temperature. The first and second laws can be combined to yield restrictions on peridynamic material models; see [2] for details.

In the next section, we will use the free energy defined by

$$\psi = \varepsilon - \theta\eta.$$

The force state can be decomposed into equilibrium and dissipative parts:

$$\underline{\mathbf{T}} = \underline{\mathbf{T}}^{equil}(\underline{\mathbf{Y}}) + \underline{\mathbf{T}}^{diss}(\underline{\mathbf{Y}}, \underline{\dot{\mathbf{Y}}}) \tag{8}$$

in which only the dissipative part contains rate dependence. It can be shown that the following identities hold:

$$\underline{\mathbf{T}}^{equil} = \psi \underline{\mathbf{Y}}, \qquad \eta = -\frac{\partial \psi}{\partial \theta}. \tag{9}$$

3. Eulerian peridynamic material modeling

In this section, we discuss a specialization of the peridynamic equations that yields, in effect, an Eulerian model for compressible fluids. The implementation of a Mie-Grüneisen equation of state is also described. The model contains both equilibrium and dissipative contributions according to the decomposition (8).

3.1. Computing bond forces from an equation of state

A nonlocal mass density $\rho(\mathbf{x}, t)$ is evaluated based on the proximity of material points in the *deformed* configuration, as opposed to the *reference* configuration. The model uses this nonlocal mass density to compute pressure, which it then translates into the force state. Let $\bar{\delta}$ denote the horizon in the deformed configuration: if points are separated by a distance greater than $\bar{\delta}$ in the deformed configuration, they do not interact.

To shorten the notation, denote a generic bond vector by $\boldsymbol{\xi}$:

$$\boldsymbol{\xi} = \mathbf{q} - \mathbf{x}.$$

Let $\omega(r)$ be a non-negative valued, continuously differentiable function on $[0, \infty)$. Assume further that

$$\omega'(\bar{\delta}) = 0 \qquad \text{and} \qquad 0 \leq r < \bar{\delta} \implies \omega'(r) < 0, \tag{10}$$

where $\omega' = d\omega/dr$, and

$$\omega(r) = 0, \qquad r \geq \bar{\delta}. \tag{11}$$

Specifically, in the following discussion we set

$$\omega(r) = (\bar{\delta} - r)^2, \qquad 0 \leq r < \bar{\delta}. \tag{12}$$

This definition of ω is chosen because it has positive second derivative; see the remarks following (21).

Let ρ_0 be the reference density of the material. Define the *nonlocal mass density* by

$$\rho(\mathbf{x},t) = \frac{\rho_0}{\gamma}\int_\Omega \omega(\underline{r}\langle\boldsymbol{\xi}\rangle)\, dV_{\mathbf{q}} \tag{13}$$

where the deformed bond length $\underline{r}\langle\boldsymbol{\xi}\rangle$ is given by

$$\underline{r}\langle\boldsymbol{\xi}\rangle = \left|\underline{\mathbf{Y}}[\mathbf{x},t]\langle\boldsymbol{\xi}\rangle\right| \tag{14}$$

and

$$\gamma = \int_\Omega \omega\left(|\boldsymbol{\xi}|\right)\, dV_{\mathbf{q}}.$$

In (13), ρ is computed from the deformed bond lengths, since, from (5) and (14),

$$\underline{r}\langle\boldsymbol{\xi}\rangle = |\mathbf{y}(\mathbf{q},t) - \mathbf{y}(\mathbf{x},t)|.$$

Because of (11), the integrand in (13) is nonzero only for points $\mathbf{q}$ within a distance $\bar{\delta}$ of the position of $\mathbf{x}$ in the *deformed* configuration. In contrast to Lagrangian material models, this may include bonds that are longer in the reference configuration than $\bar{\delta}$.

For any nonlocal mass density ρ, define the relative volume v and the compression ζ by

$$v = \frac{\rho_0}{\rho}, \qquad \zeta = \frac{\rho}{\rho_0} - 1. \tag{15}$$

Let the pressure, internal energy density, and absolute temperature of the fluid in the reference configuration be denoted p_0, ε_0, and θ_0 respectively. Assume there is a free energy function $\psi(v,\theta)$ for the material such that

$$p = -\frac{\partial\psi}{\partial v}. \tag{16}$$

The first of (9), together with the chain rule, leads to

$$\underline{\mathbf{T}}^{equil} = \psi_{\underline{\mathbf{Y}}} = \frac{\partial\psi}{\partial v}\frac{\partial v}{\partial\rho}\rho_{\underline{\mathbf{Y}}}. \tag{17}$$

To evaluate the Fréchet derivative $\rho_{\underline{\mathbf{Y}}}$, first observe that for an incremental change $\Delta\underline{\mathbf{Y}}$,

$$\Delta\underline{r}\langle\boldsymbol{\xi}\rangle = \underline{\mathbf{M}}\langle\boldsymbol{\xi}\rangle \cdot \Delta\underline{\mathbf{Y}}\langle\boldsymbol{\xi}\rangle \tag{18}$$

where $\underline{\mathbf{M}}\langle\boldsymbol{\xi}\rangle$ denotes the deformed bond direction unit vector, defined by

$$\underline{\mathbf{M}}\langle\boldsymbol{\xi}\rangle = \frac{\underline{\mathbf{Y}}\langle\boldsymbol{\xi}\rangle}{\underline{r}\langle\boldsymbol{\xi}\rangle}. \tag{19}$$

From (13), (18), and (19), it follows that

$$\begin{aligned}\Delta\rho &= \frac{\rho_0}{\gamma}\int_\Omega \omega'(\underline{r}\langle\boldsymbol{\xi}\rangle)\ \Delta\underline{r}\langle\boldsymbol{\xi}\rangle\ dV_{\mathbf{q}} \\ &= \frac{\rho_0}{\gamma}\int_\Omega \omega'(\underline{r}\langle\boldsymbol{\xi}\rangle)\ \underline{\mathbf{M}}\langle\boldsymbol{\xi}\rangle\cdot\Delta\underline{\mathbf{Y}}\langle\boldsymbol{\xi}\rangle\ dV_{\mathbf{q}}.\end{aligned}$$

From the last equation and (4), the Fréchet derivative of the nonlocal mass density is found to be

$$\rho_{\underline{\mathbf{Y}}}\langle\boldsymbol{\xi}\rangle = \frac{\rho_0}{\gamma}\omega'(\underline{r}\langle\boldsymbol{\xi}\rangle)\ \underline{\mathbf{M}}\langle\boldsymbol{\xi}\rangle. \tag{20}$$

Returning to (17), and using (15), (16), and (20), we have

$$\underline{\mathbf{T}}^{equil}\langle\boldsymbol{\xi}\rangle = \underline{t}^{equil}\langle\boldsymbol{\xi}\rangle\underline{\mathbf{M}}\langle\boldsymbol{\xi}\rangle, \qquad \underline{t}^{equil}\langle\boldsymbol{\xi}\rangle = \frac{pv^2\omega'(\underline{r}\langle\boldsymbol{\xi}\rangle)}{\gamma} \tag{21}$$

where $\underline{t}^{equil}$ is the scalar force state due to Eulerian (fluid-like) interactions. Note that the bond force is parallel to the deformed bond direction, implying that this peridynamic material model is an *ordinary* state-based model [4]. This implies that the requirement for balance of angular momentum (*nonpolarity*) is automatically satisfied without further restrictions. Since, in the second of (21), the bond force depends linearly on ω', the convexity of ω defined in (12) influences the deformation. If ω has a positive second derivative, material points that are close together tend to repel each other more strongly than those that are farther apart. This tends to help maintain equal spacing between nodes in a numerical simulation and improves stability.

Because of (10), it follows from (21) that for any bond,

$$\underline{\mathbf{T}}^{equil}\langle\boldsymbol{\xi}\rangle\cdot\underline{\mathbf{M}}\langle\boldsymbol{\xi}\rangle < 0 \quad \text{whenever} \quad p > 0.$$

That is, the bond forces are compressive if the pressure is positive. Further, by (11), the bond forces vanish if the *deformed* bond length exceeds $\bar{\delta}$. Therefore, in evaluating the integral in (13), only bonds within a neighborhood of $\mathbf{y}(\mathbf{x},t)$

with a *deformed* length less than or equal to $\bar{\delta}$ need to be included in the integration. In this sense, the material model is Eulerian in character although all the formalism is Lagrangian.

The internal energy density ε is found by integrating the energy balance (7) over time at each material point $\mathbf{x}$. The pressure p defined through (16) and the temperature θ are computed through the material model in the form $p = p(\rho, \varepsilon)$, $\theta = \theta(\rho, \varepsilon)$, where ρ is the nonlocal mass density defined in (13). In Section 3.3, we describe the particular expressions for p and θ used in the present study.

3.2. Rate-dependent bond forces

The rate-dependent term $\underline{\mathbf{T}}^{diss}$ in (8) primarily has the purpose of dissipating energy so that steady-state shocks can be modeled. Without these terms, a shock wave with a constant profile, thickness, and velocity could not satisfy the Rankine-Hugoniot relation. The dissipative term in the material model is given by

$$\underline{\mathbf{T}}^{diss}\langle\boldsymbol{\xi}\rangle = \frac{v^2}{\gamma}\Big(C_q\rho_0\mathcal{D}^2 - C_\ell\rho_0 c_0\underline{\dot{\mathbf{Y}}}\langle\boldsymbol{\xi}\rangle \cdot \underline{\mathbf{M}}\langle\boldsymbol{\xi}\rangle\Big)\underline{\mathbf{M}}\langle\boldsymbol{\xi}\rangle \tag{22}$$

where C_q and C_ℓ are dimensionless constants, the bulk wave speed c_0 is found from

$$c_0 = \sqrt{\frac{-1}{\rho_0}\frac{\partial p}{\partial v}(0)},$$

and the effective velocity change within the family $\mathcal{D}$ is defined by

$$\mathcal{D} = \frac{1}{\gamma}\int_\Omega \omega(\underline{r}\langle\boldsymbol{\xi}\rangle)\ \underline{\dot{\mathbf{Y}}}\langle\boldsymbol{\xi}\rangle \cdot \underline{\mathbf{M}}\langle\boldsymbol{\xi}\rangle\ dV_{\boldsymbol{\xi}}. \tag{23}$$

The dissipative terms after discretization are similar to artificial viscosity [15]. By testing various combinations of values of the coefficients in (22), we find that $C_q = 8$ and $C_\ell = 0.1$ usually give acceptable results.

3.3. Mie-Grüneisen equation of state

Assume that the Hugoniot has a linear dependence of the particle velocity U_p on the shock velocity U_s:

$$U_s = c_0 + SU_p \tag{24}$$

where S is a constant and c_0 is the bulk wave speed. The Mie-Grüneisen equation of state then takes the following form [16]:

$$p_{mg}(\rho,\varepsilon) = \frac{\rho_0 c_0^2 \zeta[1+(1-\Gamma_0/2)\zeta]}{[1-(S-1)\zeta]^2} + \Gamma_0(\varepsilon-\varepsilon_0), \tag{25}$$

$$\theta(\rho,\varepsilon) = \theta_0 + \frac{1}{\rho_0 C_v}(\varepsilon-\varepsilon_0) \tag{26}$$

where ζ is the compression defined in (15), Γ_0 is Grüneisen's parameter, and C_v is the specific heat at constant volume.

A simple way to account for damage that is useful when the stress level overwhelms significant effects from material strength, for example in a liquid, is to use a tensile pressure cutoff. The pressure found from the equation of state is modified according to

$$p = \max\left\{p_{mg}(\rho,\varepsilon), p_f\right\}$$

where p_f is the *fracture pressure*. For most liquids, $p_f < 0$ because the material can sustain a finite tensile hydrostatic stress without cavitating, although this stress is usually small in magnitude. An alternative approach to fracture modeling uses peridynamic bond breakage, as described below in Section 4.

3.4. Example: Ejecta from a shockwave at a free surface

An important aspect of shockwave propagation in fluids and solids is the spall and ejection of material at high velocity when the wave interacts with a free surface. Of particular interest is an irregular surface, due to the subtle interactions of incident and reflected waves that have a large effect on the breakup of material and the velocity distribution of the ejecta. This phenomenon presents challenges in computational modeling because it combines the effects of large deformations, high strain rates, and fracture. Ejection under shock loading has been studied experimentally for many years. Among the first experimental work is that of Asay [17]. Recent experimental work includes [18-22]. See [18] for a summary of the literature on experimental results. Computationally, problems of this type have been modeled successfully using the DMK-UP technique [19],

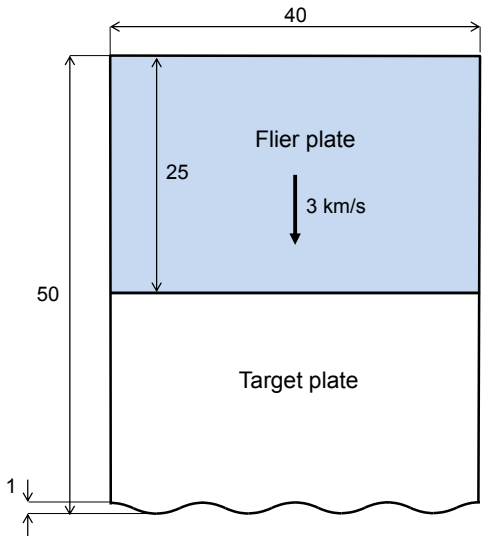

Figure 2: Diagram of the shock ejecta example problem. All spatial dimensions are in mm.

cluster dynamics [20, 21], molecular dynamics [18], and an Eulerian hydrocode [22].

In this example problem, we model an experiment by Ogorodnikov *et al.* [19] in which a shock created by an explosive plane wave generator enters an aluminum block. The shock pressure inside the block is 30GPa. The shock goes through the aluminum and reflects off the wavy free surface opposite the impact surface (Figure 2). We model this problem with the meshless Emu peridynamic code [23] modified to implement the Eulerian Mie-Grüneisen equation of state as described above. Details of the numerical method are given in the Appendix. Since Emu does not have a capability to model detonation, the shock wave is created by the symmetric impact of an aluminum flier plate on an aluminum target. The Emu model uses a square grid with a node spacing of 0.2mm and a horizon of 0.62mm. The entire two-dimensional grid contains 49,504 nodes. The time step size is $h = 0.02\mu$s. The material properties are listed in Table 1.

Parameter	*Value*	*Units*
c_0	5220	m/s
ρ_0	2700	kg/m^3
S	1.37	
Γ_0	1.97	
p_f	-500	MPa

Table 1: Material properties used in the ejecta simulation.

The initial velocity of the flier plate is 3000m/s. The impact creates a shock wave that propagates into the target with a pressure of 30GPa, a particle velocity of U_p=1500m/s, and a shock velocity of U_s=7140m/s (Figure 3). This value is acceptably close to the expected value of shock velocity from (24), which is 7230m/s, indicating that the mechanical and thermodynamic states behind the shock are being computed correctly.

The reflection of the shock from the wavy free surface creates a horizontal component of particle velocity in addition to a much larger vertical component as material is accelerated into the void. The reflected wave fronts, because they are curved, reinforce each other at some locations, causing damage to form preferentially where the surface profile was initially convex. The horizontal velocities induced near the wavy surface lead to the formation of jets. The jets form along the initially concave parts of the surface. The computed jet tip velocity is 4000m/s, compared with the measured value of 3700m/s. By the end of the calculation at 20μs, the tips of the jets start to break up.

Contours of relative density ρ/ρ_0 are plotted in Figure 4 alongside radiographs from [19]. The times of these images cannot be compared directly between the experiment and the calculation, because the initial conditions are different between the two. Nevertheless, there are clear similarities between the shapes of the jets in experiment and the model. It is also interesting that between the jets, there is low-density, low-velocity debris present in both the radiographs and the images from the model.

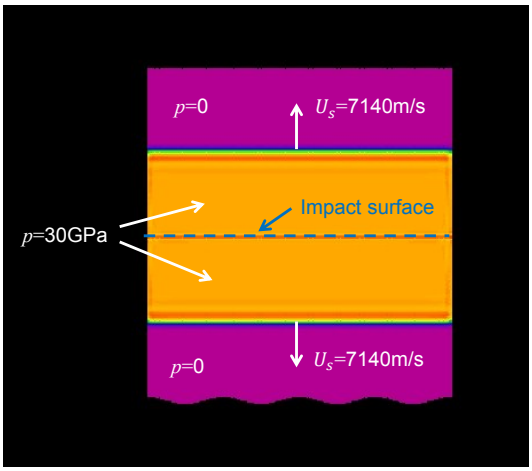

Figure 3: Shock waves in the ejecta example problem. Colors indicate pressure.

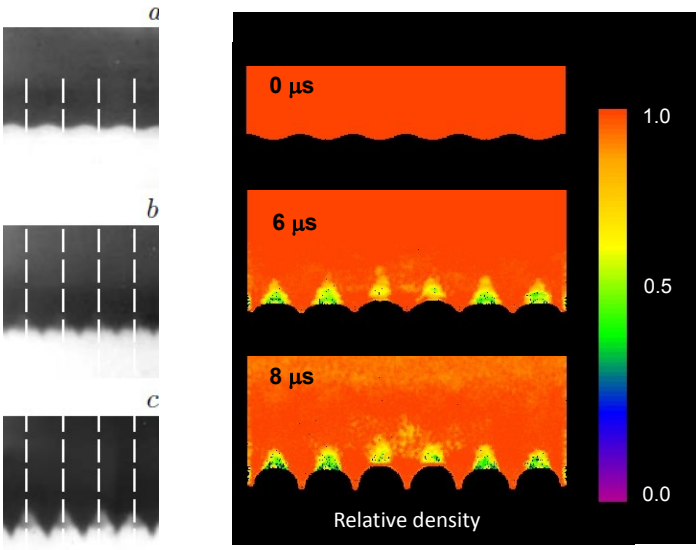

Figure 4: Left: radiographs of ejecta from an aluminum plate [19]. Right: Computed contours of relative density (ρ/ρ_0).

4. Combining Eulerian and Lagrangian components of a material model

Recall that the Eulerian formulation of the material response developed in Section 3 is really a Lagrangian formulation in which the bond force densities depend only on the current configuration. This approach makes it easy to combine the traditional form for peridynamic interactions, such as spring-like interactions between material points, with the Eulerian version. This combined approach provides a way to model phenomena such as the growth of discrete cracks with high-pressure post-failure response. As will be illustrated in an example below, this permits us to model the fragmentation of a solid followed by compression of the fragments to very high relative density.

The Eulerian contribution to the force state consists of terms in the material model that do not explicitly involve the underformed bond configurations. In the fluid model derived in Section 3, both the equilibrium and dissipative terms are Eulerian in this sense, and we write

$$\underline{\mathbf{T}}^E = \underline{t}^E \underline{\mathbf{M}} = \underline{\mathbf{T}}^{equil} + \underline{\mathbf{T}}^{diss}$$

where $\underline{\mathbf{T}}^{equil}$ and $\underline{\mathbf{T}}^{diss}$ are given by (21) and (22) respectively.

The Lagrangian contribution to the force state is included by summing the force states for the Eulerian and Lagrangian terms:

$$\underline{\mathbf{T}} = \beta \underline{\mathbf{T}}^E + (1-\beta)\underline{\mathbf{T}}^L \tag{27}$$

where β is a scalar parameter that determines the relative weighting between the Eulerian and Lagrangian terms. The Eulerian term is weighted more heavily when the compression is large; in this case, for most materials, the response is dominated by the pressure. If the Lagrangian term is ordinary (bond forces parallel to the deformed bond vectors) then we write

$$\underline{\mathbf{T}}^L = \underline{t}^L \underline{\mathbf{M}}.$$

In the following discussion, a modified form of the *microplastic* model [24] that accounts for thermal expansion is assumed for $\underline{t}^L$. For each bond $\boldsymbol{\xi}$, the bond

strain at temperature θ is defined by

$$s = \frac{|\underline{\mathbf{Y}}\langle\boldsymbol{\xi}\rangle|}{|\boldsymbol{\xi}|} - 1 - \alpha(\theta - \theta_0)$$

where α is the linear coefficient of thermal expansion evaluated at the reference temperature $\theta = \theta_0$. For a Mie-Grüneisen equation of state, α is given [16] by

$$\alpha = \frac{\Gamma_0 C_v}{3c_0^2}.$$

The bond yields under both compression and tension but breaks only in tension.

In the microplastic model, bonds respond independently of each other, like a set of nonlinear springs. Under simple shear, some bonds extend while others contract, resulting in forces that resist the shear deformation. The Poisson ratio in three dimensions is restricted to 1/4 in microplastic materials. However, any admissible Poisson ratio can be reproduced by introducing terms that explicitly respond to volume change, as in the linear peridynamic solid model [4].

The scalar force state is given by

$$\underline{t}^L\langle\boldsymbol{\xi}\rangle = \begin{cases} cs_e, & \text{if } s_e \le 0, \\ c\mu(t,\boldsymbol{\xi})s_e, & \text{if } s_e > 0 \end{cases} \tag{28}$$

where μ is a history dependent term that contains the bond damage:

$$\mu(t,\boldsymbol{\xi}) = \begin{cases} 1, & \text{if } s(t',\boldsymbol{\xi}) < s_0 \text{ for all } 0 \le t' \le t, \\ 0, & \text{otherwise.} \end{cases}$$

where s_0 is the critical bond strain for bond breakage. For any bond $\boldsymbol{\xi}$, the linear elastic part of the bond strain, denoted $s_e(t,\boldsymbol{\xi})$, is computed from

$$s_e(0,\boldsymbol{\xi}) = 0, \qquad \dot{s}_e = \begin{cases} \dot{s}, & \text{if } |s_e| \le s_y, \\ 0, & \text{otherwise.} \end{cases}$$

where s_y is the strain for bond yield (Figure 5), a constant. The spring constant c is given by

$$c = \frac{18k}{\pi\delta^4}$$

where k is the bulk modulus. Note that in the material model (28), bond damage is ignored if the bond strain is compressive.

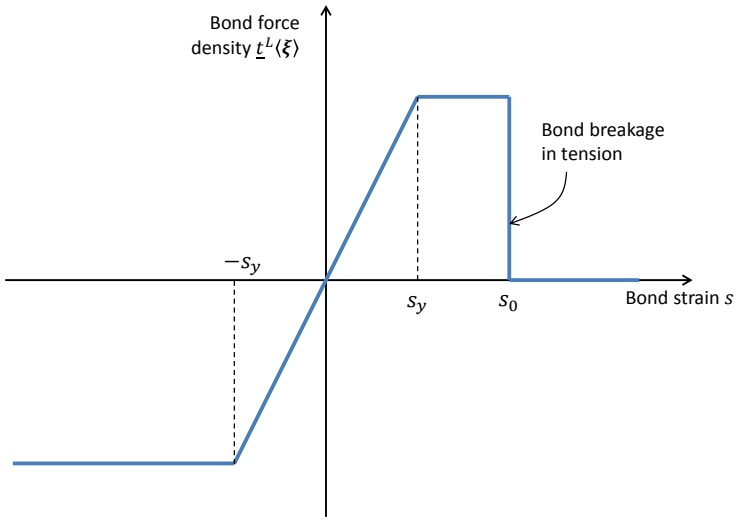

Figure 5: Material model for the Lagrangian component of the material response.

The weighting term β that appears in (27) is given by

$$\beta = \begin{cases} 4\nu - 1, & \text{if } \zeta' < 0 \quad \text{(tension)}, \\ 4\nu - 1 + (2 - 4\nu)\zeta'/\zeta_c, & \text{if } 0 \leq \zeta' \leq \zeta_c \quad \text{(small compression)}, \\ 1, & \text{if } \zeta_c < \zeta' \quad \text{(large compression)} \end{cases}$$

where ν is the Poisson ratio (for small strains), ζ_c is the compression above which the material response is taken entirely from the Eulerian term, and the compression adjusted for temperature changes is defined by

$$\zeta' = \zeta + 3\alpha(\theta - \theta_0).$$

In effect, the Poisson ratio changes continuously from ν to 1/2 as the compression increases from 0 through ζ_c.

4.1. Example: Fragmentation of a soft material followed by large compression

This example illustrates the capability described in the previous section for making a transition between a Lagrangian material model that captures features of solid response, including discrete fractures, and an Eulerian model for fluid-like response under large compressions. A cylindrical sample of diameter $D = 5$cm and height $h = 5$cm is enclosed in a rigid annular cylinder of inner diameter 7.07cm ($\approx \sqrt{2}D$). Thus, the sample is enclosed in a container that has twice the cross-sectional area as itself (Figure 6). The cylinder is compressed by a piston moving at constant velocity resulting in a global axial strain rate of 1000s^{-1}. A velocity gradient is initialized in the sample such that its velocity where it contacts the piston is the same as that of the piston. The material properties are given in Table 2. The material model is as described in the previous section, with combined Eulerian and Lagrangian contributions. The Lagrangian portion neglects plasticity, and is representative of elastomeric materials and gels. Plasticity can be incorporated into the Lagrangian portion of the material model, which is ordinary state-based, according to the method described in [4]. Details of the numerical method used in the Emu code are given in the Appendix.

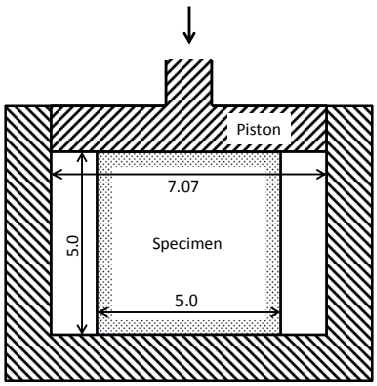

Figure 6: Initially unconfined compression of a soft brittle specimen. The sample expands laterally and eventually fills the void. All dimensions are in cm.

Parameter	*Cylinder compression*	*Wilbeck gel impact*	*LG997 gel impact*	*Units*
c_0	1000	100	100	m/s
ρ_0	1000	1000	1000	kg-m^{-3}
S_α	1.00	1.00	1.00	
Γ_0	1.60	1.60	1.60	
s_0	0.05	3.00	3.00	
s_y	0.10	0.04	0.04	
ν	0.46	0.44	0.44	
ζ_c	0.25	0.10	0.10	

Table 2: Material properties for the soft material compression and bird strike problems.

The initial response of the sample is to undergo nearly uniaxial compression. Stress concentrations near the corners of the specimen nucleate cone-shaped cracks that propagate toward the center (Figure 7). After these cracks meet each other near the center, there is no longer any radial force holding the material outside of them together. This material therefore expands suddenly into the void that initially surrounded the cylindrical sample. As this material expands radially, tensile hoop stresses within it lead to extensive fracture and fragmentation. This material failure causes a temporary drop in the net axial stress (Figure 8). After further compression, the fragments lock up with each other and the net force starts increasing again. After the piston has compressed the sample to half its original height, nearly all the void has been compressed out and further compression causes the pressure to build up more rapidly. At still larger compression, the damage and morphology of the fragments become irrelevant, and the response is completely dominated by the equation of state.

5. Application to bird strike on aircraft

Impact of a bird on an aircraft structure, or its ingestion by a jet engine, is an important safety concern in aviation. Experimental testing of the response of structures to bird strike usually uses a gelatin simulant of a roughly cylindrical shape shot by a gas gun.

Many computational results for bird strike are available in the literature (see Heimbs [25]) for a comprehensive review). Computational modeling of bird strike has largely relied on smoothed particle hydrodynamics (SPH). SPH simulations of bird strike may predict a spray of SPH nodes following impact that may not provide a realistic representation of the deformation of the bird simulant (Figure 11) [26]. From the photograph, evidently the gelatin acts somewhat like a highly compliant rubber that sustains large tensile strains without dispersing into droplets, as would be expected from a fluid. As noted in [26], the SPH simulations tend to overpredict this dispersal. This could have a detrimental effect on the accuracy of the predicted loads on an aircraft structure, creating

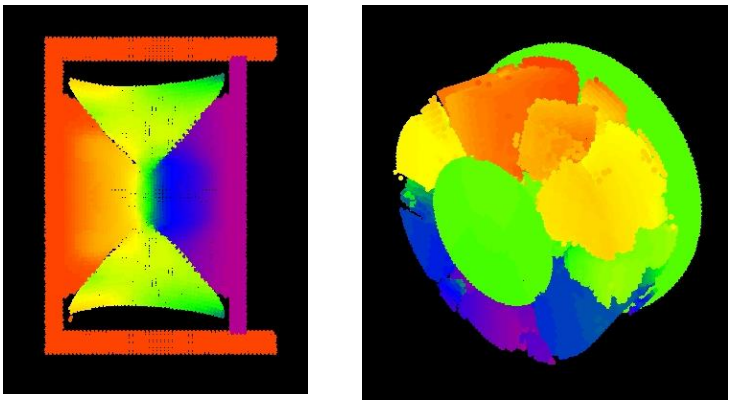

Figure 7: Formation of fragments in the soft material compression problem. Left: Initial fractures form from the corners of the specimen and propagate inward. Right: Fragments that move into the void that initially surrounded the specimen.

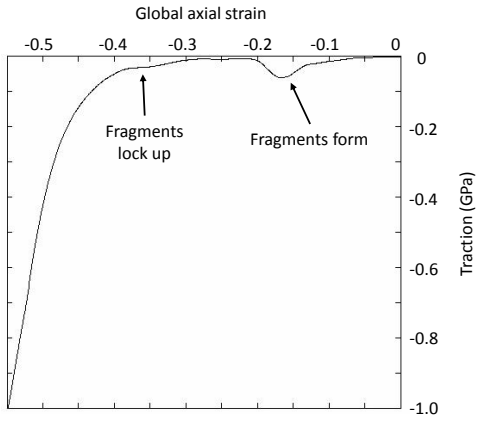

Figure 8: Net axial stress as a function of net axial strain in the gel compression problem.

a strong motivation to reduce this effect in simulations.

The numerical simulations presented in this Section use the PDBird code, which is a specialized version of the Emu peridynamic code for modeling the impact of soft projectiles. Details of the method are given in the Appendix. The thermodynamic process is treated as adiabatic, since heat conduction occurs at a negligibly slow rate relative to the mechanical deformation in high-velocity impact.

5.1. Pressure at the point of impact

As a validation test, the peridynamic model was applied to a set of experiments by Wilbeck [27]. In this set of experiments, a porous gelatin bird simulant was shot from a gas gun at a thick steel target. The simulant specimens had a variety of geometries but all were flat-ended cylinders with a length/diameter ratio of about 2. To help preserve their shape upon launch, the specimens were enclosed in sabots that were stripped before impact. The exact values of the

multiple geometries and masses, as well as the impact velocities, were apparently not reported. The target had a piezoelectric traction gauge at the point of impact. (We use the term "traction gauge" here instead of the usual term "pressure gauge" because it measures force per unit area on the target, not the hydrostatic pressure in the sample.)

A peridynamic model of a typical test by Wilbeck is shown in Figure 9. The specimen has a diameter of 0.114m and a length of L=0.228m. The meshless discretization has a grid spacing of 5.7mm with 13,680 total nodes in the projectile. The density is 1000kg-m^{-3} resulting in a mass of 2.33kg. The impact condition is normal impact at a velocity of V_0=117m-s^{-1}. The material properties are given in Table 2. A comparison of the model results against the test data for the traction at the point of impact is shown in Figure 10. The plot uses the same nondimensional variables as reported by Wilbeck in [27], which allow measurements from a variety of initial conditions and geometries to be plotted on the same set of axes.

5.2. Splash pattern

The capability described above to combine Lagrangian and Eulerian contributions in a peridynamic material model helps to reduce the spray effect in applying a particle type discretization to the bird strike problem. Rate-dependent material response, including Newtonian viscosity and other rheological effects, may also influence the impact response of gelatin, but they were not included in the peridynamic model.

Figure 12 illustrates the splash pattern predicted by a peridynamic model of this experiment, which is called LG997 in reference [26]. The projectile is a gelatin cylinder with a hemispherical front end, with a diameter of 0.096m and an overall length of 0.266m. The projectile mass is 1.81kg and the impact velocity is 170m-s^{-1}. The numerical model has a grid spacing of 4.8mm with 17,650 total nodes in the projectile. The peridynamic simulation result at 3ms shown in Figure 12 may be compared directly with the photograph in Figure 11. The peridynamic result apparently tends to preserve the coherence of the body

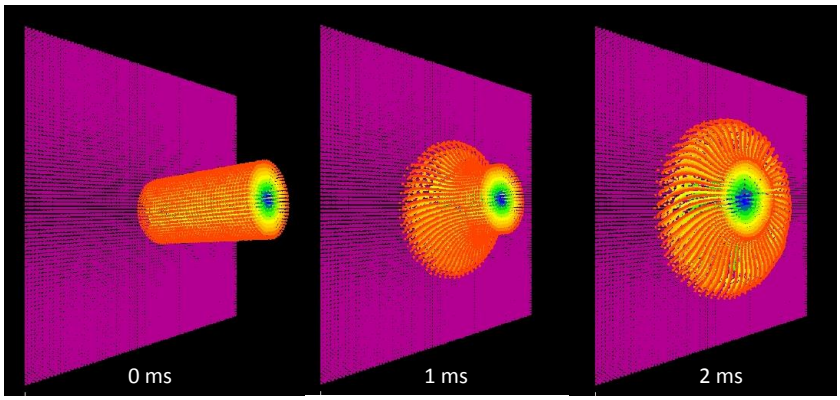

Figure 9: Snapshots of the computational grid in the simulation of the Wilbeck test [27]. with an impact velocity of 117m-s^{-1}. Colors indicate velocity magnitude.

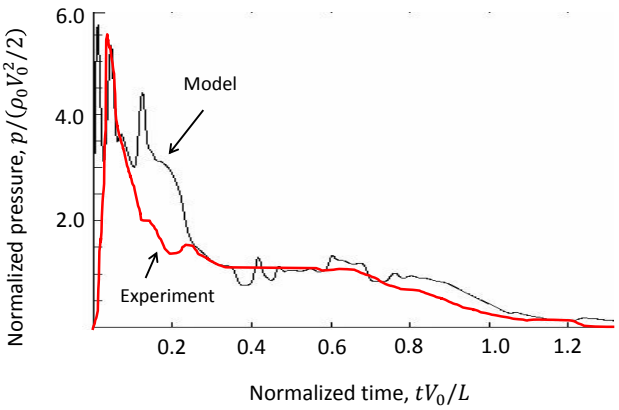

Figure 10: Normalized pressure at the point of impact in the simulation of the Wilbeck test, compared with experimental data [27]. The impact velocity is 117m-s^{-1}.

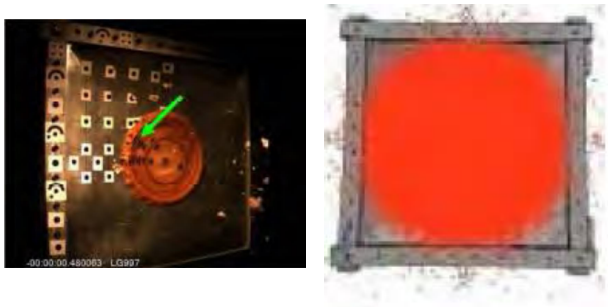

Figure 11: Photograph (left) and SPH model (right) after 3ms in the LG997 bird strike simulant impact test [26]. The arrow points to a reference mark on the specimen used to measure the deformed diameter.

(freedom from disintegration) better than SPH. The diameter of the projectile as a function of time in the peridynamic model is compared with test data and the resuts from the same SPH model, both from reference [26], in Figure 13. The peridynamic result for the deformed diameter agrees more closely with the test data than the SPH prediction does, although it is possible that some other variant of SPH would give a better result in this problem. Further discussion of the relation between SPH and particle discretization of the peridynamic equations is given in the Appendix.

5.3. Impact on a deformable target

To demonstrate application of the method to impact on a deformable target, the LG997 calculation was repeated with the rigid target replaced by a thin aluminum plate as was used in the experiment (see Section 7 of [26]). The plate was a square with a side length 1.0m and a thickness of 3.18mm. The numerical grid had a spacing of 5.7mm in both the projectile and the target, with a total of 9581 total nodes in the projectile and 153,784 in the target.

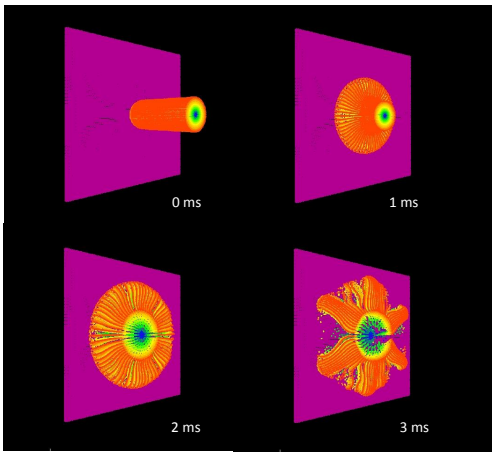

Figure 12: Splash pattern predicted by the peridynamic model of the LG997 bird strike simulant impact test.

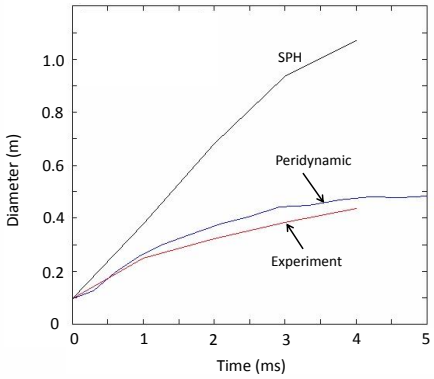

Figure 13: Time history of the diameter of the projectile in the LG997 bird strike simulant impact test.

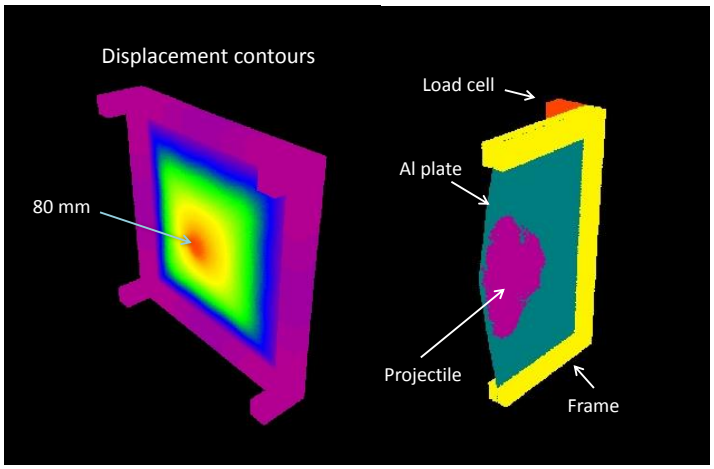

Figure 14: Predicted plate deformation due to impact of a bird simulant at the time of maximum plate deflection. Left: Contours of displacement. Right: Cut-away view of the deformed materials.

The Young's modulus of the plate was 70GPa. It was modeled as a three-dimensional peridynamic grid using a microplastic material model with force normalization [24] with a yield stress of 370MPa. The load cells and the steel frame that held the plate edges in place was also modeled as microplastic. In the model, interaction between the projectile and the target occurred through contact forces rather than peridynamic bonds. Contact forces were computed using short-range repulsive forces between the nodes of the projectile and target grids [24].

The target plate at roughly the time of peak center displacement is shown in Figure 14. The colors represent normal displacement. The time history of the center of the rear surface of the plate (near the point of impact) is shown in Figure 15 along with the measured experimental data from Section 7 of [26]).

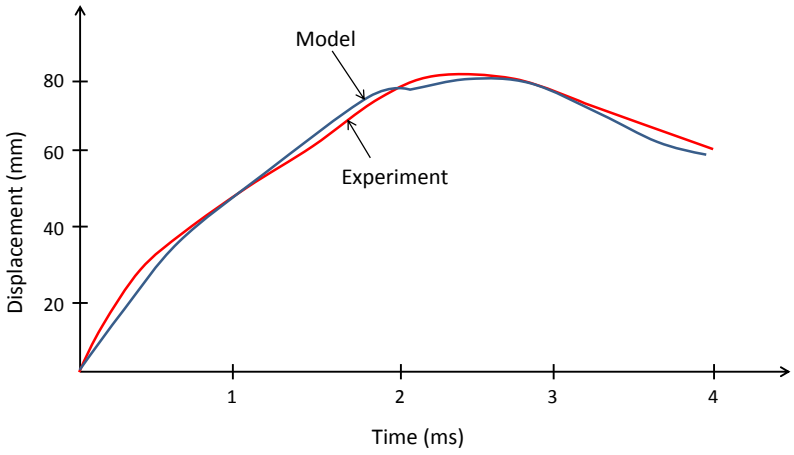

Figure 15: Predicted and experimental time histories of centerline plate deflection. Experimental data from [26].

6. Discussion

The traditional form of peridynamics, which is Lagrangian, encounters difficulties when applied to very large deformations, particularly in fluids. The root cause of these difficulties is that families become so distorted and entangled that Lagrangian material models no longer provide a reasonable physical representation of interactions between material particles. The method proposed here, which, in effect, continually redefines the family of a material particle in the deformed configuration, apparently solves this problem. The computational results demonstrate the viability of the Eulerian form of the peridynamic method for simulating large deformations of compressible fluids under high pressure and the spall of material due to shock waves. The meshless property of the method has important advantages for this application, because of the very large deformations involved and the prevalence of fracture. The ability to seamlessly combine Lagrangian (solid-like) and Eulerian (fluid-like) aspects of material response provides a way to model soft materials such as gels and post-failure response of fragmented solids.

The use of a Lagrangian and Eulerian material model in a computation requires two neighbor lists to be supplied for each node: one in the reference configuration, and another in the current configuration. The latter must be updated frequently during the calculation; this results in a modest increase in the execution time. The dual-horizon formulation of peridynamics proposed by Ren *et al.* [28] appears to be applicable to the Eulerian as well as Lagrangian parts of the model, potentially providing significant increase in computational efficiency.

Although the examples presented in this paper involve high rate deformation and impact, there is no apparently no fundamental reason why a peridynamic Eulerian fluid model could not also be applied to lower rate applications. However, in such applications, the importance of the stabilizing terms described in the Appendix would need to be evaluated relative to the physical response. Modification of the Eulerian material model to reproduce surface tension through

the incorporation of nonlocal forces between material particles is currently under investigation.

Acknowledgements

The authors gratefully acknowledge permission to use the data and results of Dr. Gerardo Olivares, National Institute for Aviation Research. Sandia National Laboratories is a multi-program laboratory operated by Sandia Corporation, a wholly owned subsidiary of Lockheed Martin Corporation, for the U.S. Department of Energy's National Nuclear Security Administration under contract DE-AC04-94AL85000. Work performed at Sandia was supported by Boeing Research and Technology through CRADA SC02/01651, by the Joint DOE/DoD Munitions Program, and through a Sandia LDRD program.

[1] S. A. Silling, Reformulation of elasticity theory for discontinuities and long-range forces, Journal of the Mechanics and Physics of Solids 48 (2000) 175–209.

[2] S. A. Silling, R. B. Lehoucq, Peridynamic theory of solid mechanics, Advances in Applied Mechanics 44 (2010) 73–168.

[3] J. Moës, J. Dolbow, T. Belytschko, A finite element method for crack growth without remeshing, Int. J. Numer. Meth. Eng 46 (1) (1999) 131–150.

[4] S. A. Silling, M. Epton, O. Weckner, J. Xu, E. Askari, Peridynamic states and constitutive modeling, Journal of Elasticity 88 (2007) 151–184.

[5] A. Agwai, I. Guven, E. Madenci, Predicting crack propagation with peridynamics: a comparative study, International Journal of Fracture 171 (2011) 65–78.

[6] E. Askari, F. Bobaru, R. Lehoucq, M. Parks, S. Silling, O. Weckner, Peridynamics for multiscale materials modeling, in: Journal of Physics: Conference Series, Vol. 125, 2008, p. 012078.

[7] J. Xu, A. Askari, O. Weckner, S. Silling, Peridynamic analysis of impact damage in composite laminates, Journal of Aerospace Engineering 21 (2008) 187–194.

[8] Y.-D. Ha, F. Bobaru, Studies of dynamic crack propagation and crack branching with peridynamics, International Journal of Fracture 162 (2010) 229–244.

[9] A. Agwai, I. Guven, E. Madenci, Damage prediction for electronic package drop test using finite element method and peridynamic theory, in: Electronic Components and Technology Conference, 2009. ECTC 2009. 59th, IEEE, 2009, pp. 565–569.

[10] P. Seleson, M. L. Parks, M. Gunzburger, R. B. Lehoucq, Peridynamics as an upscaling of molecular dynamics, Multiscale Modeling and Simulation 8 (2009) 204–227.

[11] M. L. Parks, R. Lehoucq, S. Plimpton, S. Silling, Implementing peridynamics within a molecular dynamics code, Computer Physics Communications 179 (2008) 777–783.

[12] J. A. Mitchell, A nonlocal, ordinary, state-based plasticity model for peridynamics, Tech. Rep. SAND2011-3166, Sandia National Laboratories, Albuquerque, NM (2011).

[13] J. A. Mitchell, A non-local, ordinary-state-based viscoelasticity model for peridynamics, Tech. Rep. SAND2011-8064, Sandia National Laboratories, Albuquerque, NM (2011).

[14] R. B. Lehoucq, S. Silling, Force flux and the peridynamic stress tensor, Journal of the Mechanics and Physics of Solids 56 (2008) 1566–1577.

[15] E. Caramana, M. Shashkov, W. PP, Formulations of artificial viscosity for multi-dimensional shock wave computations, Journal of Computational Physics 144 (1998) 70–97.

[16] M. A. Zocher, P. J. Maudlin, S. R. Chen, E. C. Flower-Maudlin, An evaluation of several hardening models using taylor cylinder impact data, in: Proc., European Congress on Computational Methods in Applied Sciences and Engineering, Barcelona, Spain, 2000.

[17] J. R. Asay, Material ejection from shock-loaded free surfaces of aluminum and lead, Tech. Rep. SAND-76-0542, Sandia National Laboratories, Albuquerque, NM (1976).

[18] O. Durand, L. Soulard, Large-scale molecular dynamics study of jet breakup and ejecta production from shock-loaded copper with a hybrid method, Journal of Applied Physics 111 (2012) 044901.

[19] V. A. Ogorodnikov, A. L. Mikhailov, A. V. Romanov, A. A. Sadovoi, S. S. Sokolov, O. A. Gorbenko, Modeling jet flows caused by the incidence of a shock wave on a profiled free surface, Journal of Applied Mechanics and Technical Physics 48 (2007) 11–16.

[20] V. Piskunov, I. Davydov, R. Veselov, B. Voronin, D. Demin, A. Petrov, N. Nevmerzhitskiy, V. Sofronov, Cluster dynamics method for simulation of dynamic processes of continuum mechanics, in: DYMAT-International Conference on the Mechanical and Physical Behaviour of Materials under Dynamic Loading, Vol. 2, EDP Sciences, 2009, pp. 1789–1797.

[21] I. A. Davydov, V. N. Piskunov, R. A. Veselov, B. L. Voronin, D. A. Demin, A. M. Petrov, N. V. Nevmerzhitskiy, V. N. Sofronov, Cluster dynamics method for simulation of dynamic processes of continuum mechanics, Computational Materials Science 49 (2010) S32–S36.

[22] B. A. Kullback, G. Terrones, M. D. Carrara, M. R. Hajj, M. L. Elert, W. T. Buttler, J. P. Borg, J. L. Jordan, T. J. Vogler, Quantification of ejecta from shock loaded metal surfaces, in: AIP Conference Proceedings, Vol. 1426, AIP, 2012, pp. 995–998.

[23] S. A. Silling, E. Askari, A meshfree method based on the peridynamic model of solid mechanics, Computers and Structures 83 (2005) 1526–1535.

[24] R. W. Macek, S. A. Silling, Peridynamics via finite element analysis, Finite Elements in Analysis and Design 43 (2007) 1169–1178.

[25] S. Heimbs, Computational methods for bird strike simulations: A review, Computers and Structures 89 (2011) 2093–2112.

[26] G. Olivares, Simulation and modeling of bird strike testing – phase II, Tech. Rep. NIS 09-039, National Institute for Aviation Research, Wichita, KS (2010).

[27] J. S. Wilbeck, Impact behavior of low strength projectiles, Tech. Rep. AFML-TR-77-134, US Air Force Materials Laboratory, Dayton, OH (1978).

[28] H. Ren, X. Zhuang, Y. Cai, T. Rabczuk, Dual-horizon peridynamics, International Journal for Numerical Methods in Engineering 108 (2016) 1451–1476.

[29] J. Von Neumann, R. D. Richtmyer, A method for the numerical calculation of hydrodynamical shocks, Journal of Applied Physics 21 (1950) 232–237.

[30] M. Bessa, J. Foster, T. Belytschko, W. K. Liu, A meshfree unification: reproducing kernel peridynamics, Computational Mechanics 53 (2014) 1251–1264.

[31] G. C. Ganzenmüller, S. Hiermaier, M. May, On the similarity of meshless discretizations of peridynamics and smooth-particle hydrodynamics, Computers and Structures 150 (2015) 71–78.

7. Appendix. Numerical method

In this study we use the meshless numerical approximation for the equation of motion (2) described by Silling and Askari [23], extended to state-based material models and to include the energy balance. Explicit central differencing in time is used:

$$\mathbf{y}_i^{n+1} = \mathbf{y}_i^n + h\mathbf{v}_i^{n+1/2},$$
$$\mathbf{v}_i^{n+1/2} = \mathbf{v}_i^{n-1/2} + h\mathbf{a}_i^n$$

where i is the node number, n is the time step number, and h is the time step size. In the following,

$$\boldsymbol{\xi}_{ij} = \mathbf{x}_j - \mathbf{x}_i, \quad \mathbf{r}_{ij} = \mathbf{y}_j - \mathbf{y}_i, \quad \mathbf{v}_{ij} = \mathbf{v}_j - \mathbf{v}_i, \quad r_{ij} = |\mathbf{r}_{ij}|,$$

$$\mathbf{t}_{ij} = \underline{\hat{\mathbf{T}}}[\mathbf{x}_i]\langle\boldsymbol{\xi}_{ij}\rangle, \qquad \mathbf{t}_{ji} = \underline{\hat{\mathbf{T}}}[\mathbf{x}_j]\langle\boldsymbol{\xi}_{ji}\rangle.$$

All terms in the material model $\underline{\hat{\mathbf{T}}}$ are evaluated at time step n. Volume integrals over Ω can be restricted to a smaller volume $\mathcal{E}_i^n$, which is the set of nodes j

within a distance $\bar{\delta}$ of node i in the deformed configuration at time step n. (A search must be performed at each time step to determine $\mathcal{E}_i^n$ for each node.) For example, the nonlocal density defined in (13) at node i is approximated by

$$\rho_i^n = \frac{\rho_0}{\gamma_i} \sum_{j \in \mathcal{E}_i^n} \omega(r_{ij}^n) V_j \tag{29}$$

and the equation of state takes the form

$$p_i^n = p(\rho_i^n, \varepsilon_i^n).$$

The discretized equation of motion (2) takes the form

$$\rho_0 \mathbf{a}_i^n = \sum_{j \in \mathcal{E}_i^n} (\mathbf{t}_{ij}^n - \mathbf{t}_{ji}^n) V_j + \mathbf{b}_i^n \tag{30}$$

where V_i and V_j are the volumes in the reference configuration of nodes i and j respectively. The first law expression (7) is discretized according to

$$\varepsilon_i^{n+1} = \varepsilon_i^n + h \left(\sum_{j \in \mathcal{E}_i^n} \mathbf{t}_{ij}^n \cdot \mathbf{v}_{ij}^{n+1/2} + q_i^{n+1/2} + Q_i^{n+1/2} \right).$$

The dissipative terms in the material model are discretized as follows. From (22),

$$(\underline{\mathbf{T}}^{diss})_{ij}^n = \frac{(v_i^n)^2}{\gamma_i} \Big(C_q \rho_0 (\mathcal{D}_i^n)^2 - C_\ell \rho_0 c_0 \mathbf{v}_{ij}^{n-1/2} \cdot \mathbf{M}_{ij}^n \Big) \mathbf{M}_{ij}^n \tag{31}$$

where the effective velocity change within a family defined in (23) is approximated by

$$\mathcal{D}_i^n = \frac{1}{\gamma_i} \int_\Omega \omega(r_{ij}^n) \mathbf{v}_{ij}^{n-1/2} \cdot \mathbf{M}_{ij}^n V_j.$$

The term in (31) involving $(\mathcal{D}_i^n)^2$ is simply an adaptation to peridynamics of the quadratical artificial viscosity proposed by Von Neumann and Richtmyer [29] that is standard in modern hydrocodes. The linear term involving the term $\mathbf{v}_{ij}^{n-1/2}$ is different from the usual linear artificial viscosity, because it is computed according to the rate of stretch for each bond, rather than the volumetric strain rate. This linear term stabilizes the method with respect to zero-energy modes and other unphysical modes of deformation.

The discretized expression for nonlocal density (29) is essentially the same as is used in smoothed particle hydrodynamics (SPH), raising the question of whether the present method is related to SPH. Recent work [30, 31] has examined the relationship between peridynamics and other meshless methods, including SPH, Moving Least Squares (MLS), and the Reproducing Kernel Particle Method (RKPM). These studies show that the particle type discretization of the peridynamic continuum equations, under certain severe restrictions, is essentially the same as these earlier methods. These restrictions include the use of a special class of peridynamic material models (*correspondence* materials, which are a subclass of the non-ordinary state-based materials). The restrictions also include that there be no bond damage, and no bond forces of the type described in Section 4. Since the fluid model proposed in Section 3 is a type of ordinary, rather than non-ordinary, state-based material model, it is not yet clear whether the results in [30, 31] apply in this case. The peridynamic model rigorously enforces the balance of angular momentum. Also, since the thermodynamic form of peridynamics discussed in Section 2.2 is fully consistent with the mechanical theory, the particle discretization inherits this consistency.